

# Quantitative Investigation of Imaging Quality vs. Radar Position Errors in Millimeter-wave SAR

1<sup>st</sup> Qi Wen

*Department of Electrical & Computer Engineering  
The University of Arizona  
Tucson, AZ 85719, USA  
qiwen@arizona.edu*

2<sup>nd</sup> Siyang Cao

*Department of Electrical & Computer Engineering  
The University of Arizona  
Tucson, AZ 85719, USA  
caos@arizona.edu*

**Abstract**—Millimeter wave (mmWave) imaging has promising potential for many applications because of its fine resolution, object-penetration capabilities, and all-weather, all-day working conditions. Combined with low-cost mmWave radars, the synthetic aperture radar (SAR) technique enables flexible, cost-effective, mmWave imaging solutions. This paper experimentally investigates how SAR imaging quality depends on in-aperture 2D Gaussian position errors. We emulate a wide range of position errors with root-mean-square values ranging from 1 mm up to 256 mm, covering between a fraction and a few tens of the wavelengths at 77 GHz. The presented results provide useful guidance for designing portable mmWave SAR systems that can benefit from flexible and low-cost motion tracking solutions. The data and code are publically shared at <https://github.com/radar-lab/SAR.git>.

**Index Terms**—Millimeter-wave imaging, synthetic aperture radar (SAR), Range Doppler Algorithm (RDA), tracking errors

## I. INTRODUCTION

Millimeter wave (mmWave) imaging has drawn significant attention in recent years, because of mmWaves' unique physical characteristics and continuously reduced cost of mmWave radars. Spanning from 10 to 1 mm in wavelength (30 to 300 GHz in frequency), mmWaves enable sub-degree diffraction-limited resolution with an aperture no larger than a few tens of centimeters, and have penetration capabilities through fog/rain/cloud and various optically-opaque materials. As a result, mmWave imaging has been demonstrated suitable for a wide range of applications including security inspection [1], [2], medical diagnosis [3], [4], non-destructive testing [5], autonomous driving [6], [7], and unmanned aerial vehicle (UAV) based remote sensing [8]. In addition, the rapid advancement in solid-state technologies in recent decades has empowered highly-integrated radar systems with significant cost reduction [9]. The low cost of commercially available mmWave radars nowadays catalyzes more research and commercialization activities around mmWave imaging.

Synthetic aperture radar (SAR) technique [10], [11] provides a cost-effective and flexible approach for mmWave imaging. Because imaging resolution is inversely proportional to aperture size, having a large aperture helps achieve fine resolutions. SAR forms a large virtual aperture by moving a radar relative to the targets, and generates high-resolution imagery via processing all the radar echos acquired across the

aperture. Compared to physically constructed large-aperture instruments, SAR reduces the cost and complexity of mmWave imaging, though at some expense of integration time and signal processing. The working principles of SAR make it attractive to applications that desire portable solutions for mmWave imaging: for example in self-driving cars and UAVs, the space and load capacities are tightly constrained; hand-held or wearable mmWave imaging devices also become viable.

One key requirement for SAR is accurate knowledge of instantaneous radar positions during data acquisition. Many research groups have developed mmWave SAR imaging systems using motorized linear rails and commercially available 60 or 77 GHz radars [12]–[15]. In these systems, the radar positions were either directly recorded by motion controllers, or were tracked by a high-precision marker-based optical tracking system. The radar position errors in their experiments, which were mostly determined by imperfect synchronization between radar and motion system, were negligible compared to the radar wavelengths ( $\sim 4$  mm at 77 GHz; 5 mm at 60 GHz). In many practical applications, however, it is desirable to move the radar using an ego-vehicle or by hand, while tracking the motion accurately to implement SAR. Depending on tracking systems, the position errors could be a few millimeters, i.e. comparable to the radar wavelength, or at the order of centimeters. For example, authors in [16] have developed a cost-effective pen-like tracking system by fusing the data from ultra-wideband radios and inertial measurement unit (IMU); they achieved a median position error of 2.9 mm over an area of  $2.5 \text{ m} \times 2 \text{ m}$ . Authors in [6] demonstrated centimeter-level positioning accuracy for autonomous vehicles by fusing multiple onboard sensors including Global Navigation Satellite System (GNSS), IMUs, odometers, and steering angle sensors. It is noted that some optical tracking systems, such as Optitrack [17] and Vicon [18], can track motions with sub-millimeter accuracy. But they are expensive and require sufficient line-of-sight visibility.

Hence for designing practical portable mmWave SAR systems, a quantitative understanding of the relationship between SAR imaging results and radar position errors can be valuable. Especially for applications that need real-time or quasi real-time imaging, it may be challenging to implement motion compensation or auto-focusing techniques due to optimization

load [19]. In previous studies of mmWave SAR imaging, there is a lack of quantitative measures of imaging quality, and to our knowledge, no dedicated investigation on the effects of position errors exists. The work presented here is to address these issues.

In this paper, we discuss an experimental investigation of how radar position errors affect mmWave SAR imaging. We develop a SAR testbed that moves a 77 GHz frequency-modulated continuous wave (FMCW) radar to form synthetic apertures. We emulate position errors by shuffling the synchronization. For demonstration purposes, the Range Doppler Algorithm (RDA) has been adopted for generating SAR imagery. The SAR imaging quality is quantified using entropy and contrast to provide both quantitative and qualitative insights about the results. In addition, we will share our data and code at <https://github.com/radar-lab/SAR.git>.

The structure of the rest of the paper is as follows. In Sec. II, we review the signal model and RDA, and explain in detail how we emulate the position errors using experimental data. We give a brief summary of the experimental hardware and data acquisition process in Sec. III. In Sec. IV, we present the results from our experiment and provide a detailed discussion on the behaviors of imaging quality vs. position errors. We give our conclusions at the end.

## II. METHODS

### A. Radar Signal Model and RDA

To aid the readers and to clarify assumptions that we use in our work, in this section we briefly review the relevant radar signal model and the SAR processing algorithm RDA.

We use an FMCW radar that sends out linear frequency modulated (LFM) signal as a function of fast time  $t$ :

$$s_t(t) = \cos(2\pi f_0 t + \pi K t^2), \quad 0 \leq t \leq T_{up}, \quad (1)$$

where  $f_0$  is the starting frequency, and the chirp rate  $K$  is equal to the bandwidth  $B$  divided by the up-chirp time  $T_{up}$ .

Suppose that at slow time  $\eta$ , a point target locates at a distance  $R(\eta)$  from the radar. The round-trip time delay  $\tau$  hitting this target is thus equal to  $2R(\eta)/c$ , where  $c$  is the speed of light. Here we assume a monostatic-radar model, i.e. the transmit and receive antennas are at the same location. Therefore, the received echo is:

$$s_r(t, \eta) = \sigma \cos[2\pi f_0(t - 2R(\eta)/c) + \pi K(t - 2R(\eta)/c)^2], \quad (2)$$

where  $\sigma$  represents the received signal amplitude, which is affected by target reflectivity, wave propagation decay, and beam pattern; in the case of SAR, all of these physical phenomena may vary with respect to  $\eta$  due to the relative motion between the radar and the target.

After "de-chirping", a common stretch processing technique that mixes the received signal with the I (in-phase) and Q (quadrature) components of the transmit signal, the received signal becomes:

$$s(t, \eta) = \sigma e^{-j2\pi[2f_0 R(\eta)/c + 2KtR(\eta)/c - 0.5K(2R(\eta)/c)^2]} \quad (3)$$

$$\approx \sigma e^{-j4\pi f_0 R(\eta)/c} e^{-j2\pi(2KR(\eta)/c)t} \quad (4)$$

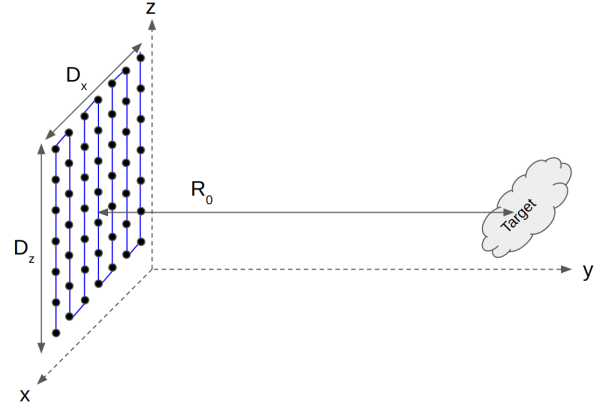


Fig. 1: The geometry of the SAR configuration. The radar boresight is toward the  $+y$  direction. The SAR aperture of size  $D_x$  by  $D_z$  is formed on the  $xz$  plane by moving the radar along the blue pattern. The black dots represent the radar spacial samplings, at each of which a radar chirp is sent out and received. The target is at  $y = R_0$ .

We ignore the last phase term in eq. (3), which only counts for about 0.004 radians in our experiment. The parameters of our experiment are summarized later in Tab. I in Sec. III-B.

The RDA is a family of SAR algorithms that process range and cross-range separately while taking advantage of the computation efficiency in the frequency domains via FFT [10], [11]. The RDA performs the range cell migration corrections (RCMC) in the range-Doppler domain. In our work, we implement the low-squint case of RDA, which simplifies processing by assuming that the synthetic aperture is small compared to the target range. Fig. 1 illustrates the SAR configuration and geometries in our experiment: the synthetic aperture size is  $D_x = D_z = 40$  cm, and targets are positioned about  $R_0 = 1$  m away. Despite the fact that this aperture size is not really small compared to the range, after experimenting we concluded that the low-squint RDA is sufficient to generate SAR images that are sharp enough for the current study. This result may be explained by an effectively smaller aperture in the experiment due to beam pattern and specular reflection [20], a topic that is beyond the scope of this paper.

We rewrite the radar-target range  $R(\eta)$  as:

$$R(\eta) = \sqrt{R_0^2 + (v_x \eta)^2 + (v_z \eta)^2}, \quad (5)$$

where  $v_x$  and  $v_z$  are the spacial sampling speed in meters per second in the  $x$  and  $z$  directions respectively. We have chosen a reference of  $\eta$  such that  $R(\eta = 0) = R_0$ , i.e. when the radar boresight is right through the target. If we assume that the SAR aperture is small compared to  $R_0$ , then

$$R(\eta) \approx R_0 + \frac{v_x^2}{2R_0} \eta^2 + \frac{v_z^2}{2R_0} \eta^2. \quad (6)$$

Plugging eq. 6 back into eq. 4, we get:

$$s(t, \eta) \approx \sigma e^{-j4\pi \frac{R_0}{\lambda}} e^{-j\pi K_{ax} \eta^2} e^{-j\pi K_{az} \eta^2} e^{-j2\pi(2KR(\eta)/c)t}, \quad (7)$$

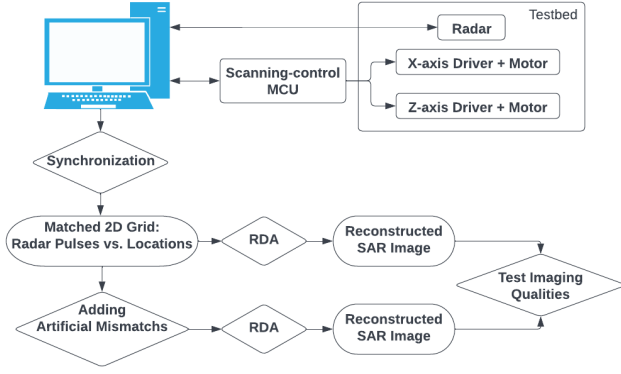


Fig. 2: The overall framework of the experiment.

where  $\lambda$  is the wavelength, and  $K_{ax} = \frac{2v_x^2}{R_0\lambda}$ ,  $K_{az} = \frac{2v_z^2}{R_0\lambda}$  are the LFM rates in slow time  $\eta$  along x and z directions respectively.

To implement RDA given the signal model in eq. 7, we first use FFT over the fast time  $t$  for range compression and then use matched filters in the x and z directions separately over the slow time  $\eta$  for cross-range compression. The matched filtering is done in the Doppler domain by an FFT/inverse-FFT process with reference signals constructed using  $K_{ax}$  or  $K_{az}$ . The range cell migrations are negligible compared to the range bin resolution in our experiment. Reference [21] provides helpful guidance for implementing low-squint RDA.

### B. Emulation of Position Errors

Fig. 2 shows the overall framework of our experiment. The uniform radar spacial samplings, as shown in Fig. 1, are achieved by utilizing two perpendicular motorized linear stages, and by proper synchronization between radar chirps and locations. For instance, the scanning-control system outputs timestamps  $t_i$  and radar positions  $(x_i, z_i)$  on the synthetic aperture plane, while radar system outputs timestamps  $\eta_i$  and chirp signals  $s(\eta_i)$ . The timestamps of both systems are referenced to the common laptop's clock. For any position  $(x_i, z_i)$  on the 2D grid shown in Fig. 1, one can synchronize it to a corresponding radar chirp  $s(\eta_i)$  such that  $\eta_i$  is the closest timestamp to  $t_i$ . With proper choices of timestamp intervals, the synchronization errors in terms of distance can be controlled to a negligible amount compared to the radar wavelength.

In practical applications with no precise motion control platform, however, the position errors due to inaccurate motion tracking lead to considerable distortions of SAR signal at dance gamel. To illustrate, let us assume a chirp  $\tilde{s}(\tilde{\eta}_j)$  that is sent out and received at a real position  $(x_j, z_j)$  on the aperture plane. Due to motion tracking errors, this chirp  $\tilde{s}(\tilde{\eta}_j)$  may be mistakenly registered with position  $(x_i, z_i)$  instead.

To emulate this kind of position errors and study their effects in SAR imaging, we add artificial mismatches between the radar chirps and positions to our synchronized experimental data. After the initial synchronization, we have a 2D spacial

grid where each point has a corresponding chirp signal. To add mismatches on top of this baseline synchronization, at each location  $(x_i, z_i)$  on this grid, we register the radar signal  $\tilde{s}(\tilde{\eta})$  that was originally synchronized to another grid location  $(x_j, z_j)$ . The location  $(x_j, z_j)$  is randomly picked such that the displacement  $(\Delta x_i, \Delta z_i) = (x_j - x_i, z_j - z_i)$  follows an underlying 2D Gaussian distribution as follows,

$$\Delta x_i \sim \mathcal{N}(0, \frac{\tilde{l}^2}{2}), \Delta z_i \sim \mathcal{N}(0, \frac{\tilde{l}^2}{2}), \quad (8)$$

where  $\tilde{l}$  is the root mean square (RMS) of the position errors to emulate. Note that for those randomly picked points that are outside the aperture grid, we pick their closest in-aperture points as an approximation.

### C. Imaging Quality Measures

We use entropy and contrast to quantify SAR imaging quality. Following [22], the entropy and contrast of an image  $g(k, n)$  with size  $M \times N$  are defined as:

$$\text{entropy} = - \sum_{k=0}^{M-1} \sum_{n=0}^{N-1} \frac{|g(k, n)|^2}{S} \ln \frac{|g(k, n)|^2}{S}, \quad (9)$$

$$\text{contrast} = \sqrt{\frac{MN}{S^2} \sum_{k=0}^{M-1} \sum_{n=0}^{N-1} |g(k, n)|^4 - 1}, \quad (10)$$

where

$$S = \sum_{k=0}^{M-1} \sum_{n=0}^{N-1} |g(k, n)|^2. \quad (11)$$

For the same scene, better SAR technique results in a sharper image, and thus smaller entropy and larger contrast.

## III. EXPERIMENT

### A. SAR Testbed

We develop a SAR testbed, as shown in Fig. 3. This testbed physically consists of two sub-systems: (1) a low-cost 2D

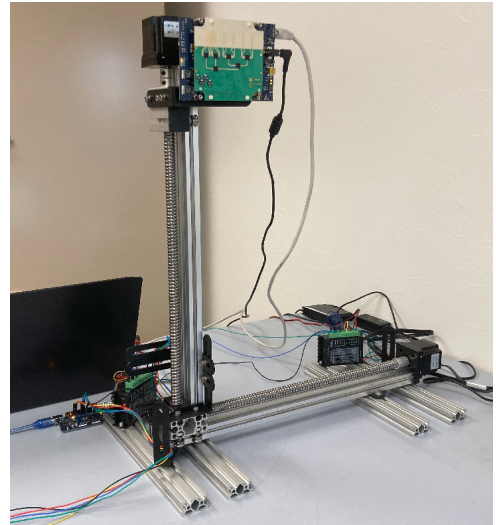


Fig. 3: The SAR testbed.

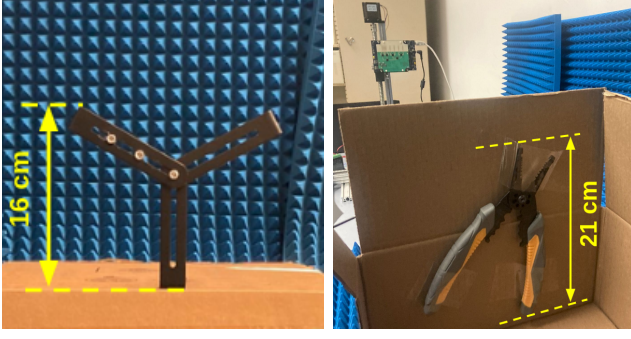


Fig. 4: Left: a carbon steel Y-shape model. Right: a wire stripper obstructed by cardboard (photo was taken from the back of the cardboard looking toward the radar).

motion-control system and (2) INRAS Radarbook platform with a 77 GHz frontend [23].

For the 2D motion-control system, two 400 mm ball-screw linear stages are mounted perpendicular to each other and are motorized by NEMA23 stepper motors. We use a microcontroller unit (MCU) Arduino Mega 2560 to control two TB6600 drivers, each of which triggers the radar motions in one axis. The MCU is connected to a laptop via USB, and we use ROS package “roserial\_arduino” [24] to log the motion data into the laptop. This motion-control system is capable of moving the radar stably up to 20 mm/s with a position precision at an order of 0.01 mm, and cost less than \$300 to build.

The Radarbook is connected to the laptop via ethernet and can directly output radar’s raw analog-to-digital conversion (ADC) data into the laptop. The 77 GHz multiple-input multiple-output (MIMO) frontend has 4 transmit and 8 receive antennas. In our experiment, we only use 1 transmit and 1 receive for simplicity.

#### B. Data Acquisition

Target objects, among which two examples are shown in Fig. 4, are positioned at a distance of roughly 1 meter in front of the SAR testbed. The parameters of the experiment are summarized below in Tab. I. Note that we choose to sample every 1 mm in both x and z directions over the aperture plane, corresponding to a  $\lambda/4$  spacial sampling interval which guarantees Nyquist criterion even in the ‘worst’ possible case when  $R_0 = 0$  as discussed in [1].

TABLE I: The parameters of the experiment.

Parameter	Value
Frequency band	76-78 GHz
Up-chirp duration ( $T_{up}$ )	64 $\mu$ s
Chirp rate ( $K$ )	31.25 MHz/ $\mu$ s
ADC samples per chirp	256
Synthetic aperture ( $D_x, D_z$ )	0.4 m x 0.4 m
Aperture-target distance ( $R_0$ )	1 m
Scan speed	20 mm/s
Spacial sampling interval	1 mm (x & z)

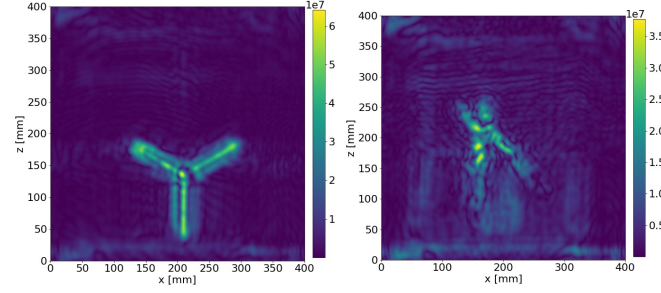


Fig. 5: Imaging results of the target objects using the baseline synchronization.

## IV. RESULTS AND DISCUSSION

### A. Imaging with No Artificial Mis-match

We estimate the position errors of the ‘baseline’ synchronization, i.e. without adding any artificial mismatches, using the timestamps and scan speed. The RMS of the baseline errors is about 0.25 mm, a value that is much smaller than the artificial mismatches that we will add later. One could further reduce the synchronization error by having shorter radar pulse repetition intervals.

We successfully reconstruct SAR images using the RDA method discussed in Sec. II-A. Fig. 5 shows the imaging results of the target objects shown in Fig. 4. It can be seen that the edges of the objects are reasonably clear, and those 6 mm-wide slots in the Y-shape model are visible too. When comparing to a theoretical resolution of SAR  $\lambda R_0/2D = 4.9$  mm [10], these experimental imaging results are acceptable. The imaging quality is quantified in Tab. II.

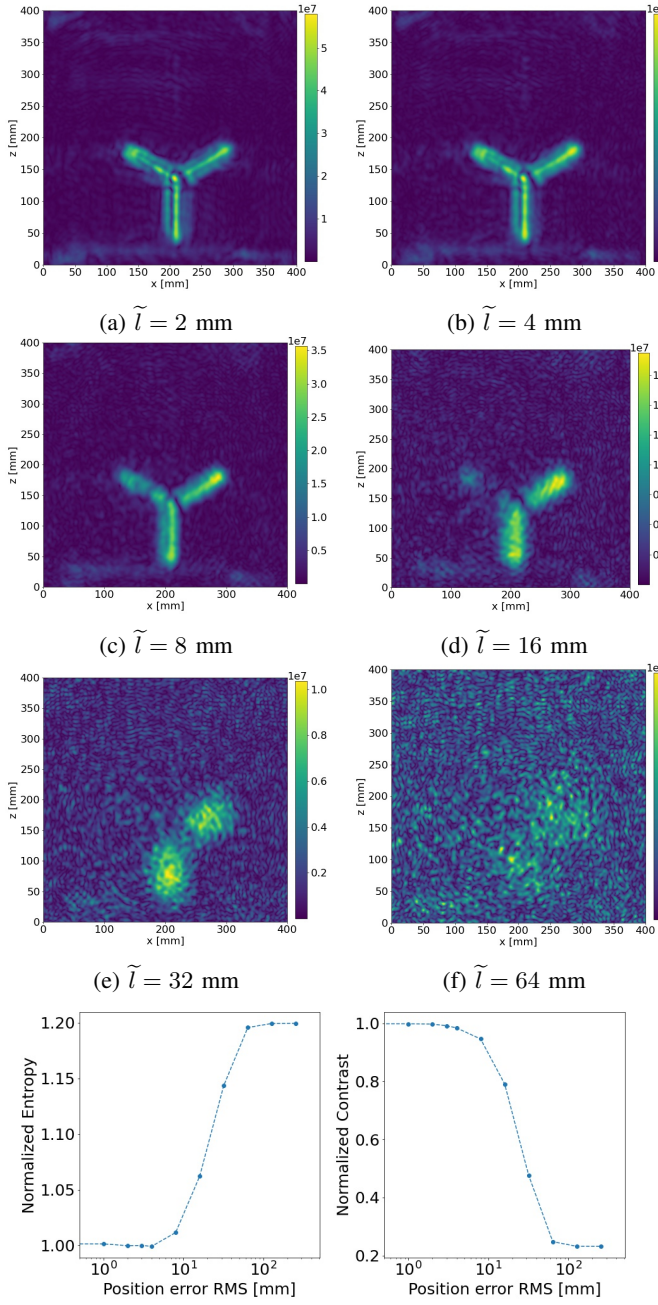
### B. Imaging Quality vs. Position Errors

To emulate position errors, we re-shuffle the baseline synchronization by adding artificial mismatches between the radar data and the position data, as explained in Sec. II-B. We test a wide range of RMS of the position errors  $\tilde{l}$  from 1 mm up to 256 mm. More specifically, for each selected value of  $\tilde{l}$ , we randomly generate spatial displacements at all grid locations following a 2D Gaussian distribution described by eq. 8, and then we mismatch the radar data obtained at those displaced locations to the original locations. This procedure gives us a new inaccurate synchronization between radar data and position data, and thus emulates the effects of 2D Gaussian position errors on the aperture plane. A more rigorous description of this mismatch procedure can be found in Sec. II-B. Given the emulation of position errors for each  $\tilde{l}$ , we repeat the SAR imaging processing and imaging quality

TABLE II: The imaging quality measures of the baseline results ( $\tilde{l} = 0$ ).

Target Object	Entropy	Contrast
Y-shape model	9.7	4.3
Obstructed wire stripper	10.7	2.9



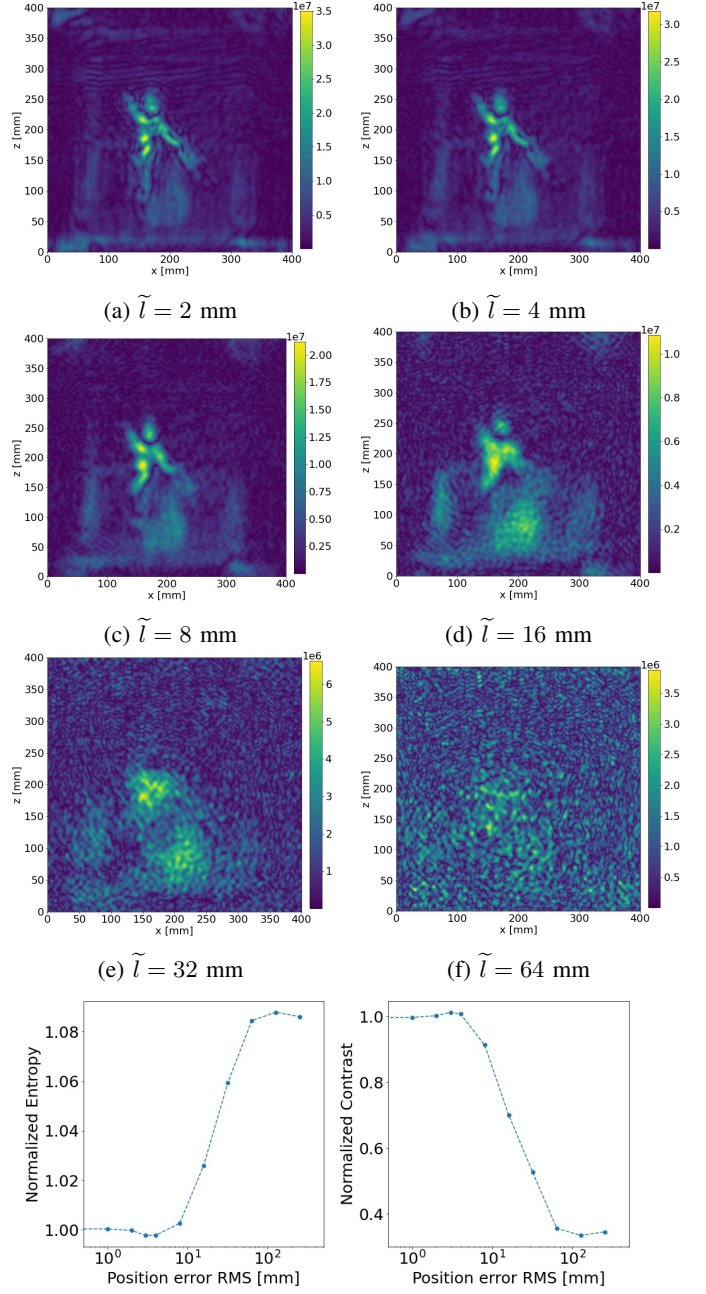


(g) Normalized entropy and contrast vs. position errors.

Fig. 6: Imaging results of the Y-shape model vs. position error RMS  $\tilde{l}$ .

test. Fig. 6 and Fig. 7 show some examples of the final imaging for various  $\tilde{l}$ . In the same figures, we also show the entropy and contrast normalized to the baseline results (Tab. I) vs.  $\tilde{l}$  on a logarithmic scale. Below we present further discussions on these results.

First of all, it is not surprising to observe degradation of imaging qualities as we increase  $\tilde{l}$ . A larger  $\tilde{l}$  means a more inaccurate estimation of radar sampling positions, thus leading to more distortions in the SAR signal. Especially at very large



(g) Normalized entropy and contrast vs. position errors.

Fig. 7: Imaging results of the obstructed wire cutter vs. position error RMS  $\tilde{l}$ .

$\tilde{l}$ , e.g. when  $\tilde{l} = 64$  mm, the spatial information of the targets is almost completely lost, resulting in noise-dominant images. Therefore, the entropy and contrast plateau to constant values at large  $\tilde{l}$ .

The interesting behaviors at low  $\tilde{l}$  are worth further discussion. In our experiment, the imaging results barely change when the position error  $\tilde{l}$  is less than 4 mm, which is about one wavelength. Even at about two wavelengths  $\tilde{l} = 8$  mm, the imaging results still give a lot of useful information about

the objects. For example, if we compare the imaging (c) in Fig. 6 to the baseline result of the Y-shape object shown in Fig. 5, one can still easily identify most of the edges and slots. This immunization to small position errors is also illustrated by the plots of normalized entropy and normalized contrast vs.  $\tilde{l}$ : the variations at low  $\tilde{l}$  are small.

The physical explanation of the imaging quality behaviors at low  $\tilde{l}$  is in fact very simple. Recall that we have fixed the aperture on the xz-plane and the position errors are defined in the aperture. Since the distance between the aperture and targets  $R_0 = 1$  m is fixed, a small change of position in the xz plane does not affect much the radar-target range  $R(\eta)$ , the quantity that ultimately determines the phase (and the amplitude) of the signal as discussed in Sec. II-A. This explanation indicates that for  $R_0$  larger than 1 m, the tolerance on  $\tilde{l}$  would be even larger. In fact, authors in [6] demonstrated that centimeter-level position accuracy enabled high-resolution mmWave SAR imaging in driving scenarios where objects were well beyond 1 m away from the radar.

Despite the simple explanations discussed above, we believe that the demonstrated behaviors of the SAR imaging quality vs. position errors serve as useful guidance for designing practical mmWave SAR systems. For example, if one wants to design a low-cost, real-time, handheld, mmWave imaging device, constraining the radar spacial samplings on a physical plane, and adopting a low-cost motion tracking solution that has an accuracy of a few millimeters (e.g. the one demonstrated in [16]), is probably a viable option. In such an application, one may also want to consider the aids from compressed sensing and deep learning to further relax the operation requirements and to enhance imaging qualities [15], [25].

## V. CONCLUSION

In this paper, we discussed our experimental investigation of how mmWave SAR imaging quality is affected by radar position errors. By leveraging the data collected from a SAR testbed, we emulated position errors and systematically compared the imaging results. The demonstrated quantitative behaviors of the imaging quality vs. position errors, as well as the related discussions, may provide helpful guidance for designing portable mmWave SAR systems.

## REFERENCES

- [1] D. M. Sheen, D. L. McMakin, and T. E. Hall, "Three-dimensional millimeter-wave imaging for concealed weapon detection," *IEEE Transactions on microwave theory and techniques*, vol. 49, no. 9, pp. 1581–1592, 2001.
- [2] S. S. Ahmed, "Microwave imaging in security—two decades of innovation," *IEEE Journal of Microwaves*, vol. 1, no. 1, pp. 191–201, 2021.
- [3] S. Di Meo, P. F. Espin-Lopez, A. Martellosio, M. Pasian, G. Matrone, M. Bozzi, G. Magenes, A. Mazzanti, L. Perregrini, F. Svelto *et al.*, "On the feasibility of breast cancer imaging systems at millimeter-waves frequencies," *IEEE Transactions on Microwave Theory and Techniques*, vol. 65, no. 5, pp. 1795–1806, 2017.
- [4] F. Topfer and J. Oberhammer, "Millimeter-wave tissue diagnosis: The most promising fields for medical applications," *IEEE Microwave Magazine*, vol. 16, no. 4, pp. 97–113, 2015.
- [5] K. Brinker, M. Dvorsky, M. T. Al Qaseer, and R. Zoughi, "Review of advances in microwave and millimetre-wave ndt&e: Principles and applications," *Philosophical Transactions of the Royal Society A*, vol. 378, no. 2182, p. 20190585, 2020.
- [6] D. Tagliaferri, M. Rizzi, M. Nicoli, S. Tebaldini, I. Russo, A. V. Monti-Guarnieri, C. M. Prati, and U. Spagnolini, "Navigation-aided automotive sar for high-resolution imaging of driving environments," *IEEE Access*, vol. 9, pp. 35 599–35 615, 2021.
- [7] S. Tebaldini, M. Rizzi, M. Manzoni, A. M. Guarnieri, C. Prati, D. Tagliaferri, M. Nicoli, U. Spagnolini, I. Russo, and C. Mazzucco, "Sar imaging in automotive scenarios," in *2022 Microwave Mediterranean Symposium (MMS)*. IEEE, 2022, pp. 1–5.
- [8] W.-Q. Wang, Q. Peng, and J. Cai, "Waveform-diversity-based millimeter-wave uav sar remote sensing," *IEEE Transactions on Geoscience and Remote Sensing*, vol. 47, no. 3, pp. 691–700, 2009.
- [9] J. Lin, C. Li, C.-C. Chang, T.-H. Tsai, D. Zito, and S.-F. Chang, "Review—semiconductor integrated radar for sensing applications," *ECS Journal of Solid State Science and Technology*, vol. 7, no. 7, p. Q3126, 2018.
- [10] M. A. Richards, *Fundamentals of radar signal processing*. McGraw-Hill Education, 2014.
- [11] I. G. Cumming and F. H. Wong, "Digital processing of synthetic aperture radar data," *Artech house*, vol. 1, no. 3, pp. 108–110, 2005.
- [12] G. Alvarez-Narciandi, M. Lopez-Portugues, F. Las-Heras, and J. Laviada, "Freehand, agile, and high-resolution imaging with compact mm-wave radar," *IEEE Access*, vol. 7, pp. 95 516–95 526, 2019.
- [13] M. E. Yanik, D. Wang, and M. Torlak, "Development and demonstration of mimo-sar mmwave imaging testbeds," *IEEE Access*, vol. 8, pp. 126 019–126 038, 2020.
- [14] S. Wei, Z. Zhou, M. Wang, J. Wei, S. Liu, J. Shi, X. Zhang, and F. Fan, "3dried: A high-resolution 3-d millimeter-wave radar dataset dedicated to imaging and evaluation," *Remote Sensing*, vol. 13, no. 17, p. 3366, 2021.
- [15] H. Regmi, M. S. Saadat, S. Sur, and S. Nelakuditi, "Squigglemilli: Approximating sar imaging on mobile millimeter-wave devices," *Proceedings of the ACM on Interactive, Mobile, Wearable and Ubiquitous Technologies*, vol. 5, no. 3, pp. 1–26, 2021.
- [16] Y. Cao, A. Dhekne, and M. Ammar, "Itracku: tracking a pen-like instrument via uwb-imu fusion," in *Proceedings of the 19th Annual International Conference on Mobile Systems, Applications, and Services*, 2021, pp. 453–466.
- [17] "OptiTrack," <https://optitrack.com/>, accessed: 2022-10-19.
- [18] "Vicon," <https://www.vicon.com/>, accessed: 2022-10-19.
- [19] J. Chen, M. Xing, H. Yu, B. Liang, J. Peng, and G.-C. Sun, "Motion compensation/autofocus in airborne synthetic aperture radar: A review," *IEEE Geoscience and Remote Sensing Magazine*, vol. 10, no. 1, pp. 185–206, 2021.
- [20] C. Liu, "Influence of antenna pattern on synthetic aperture radar (sar) imaging and complex permittivity extraction from images of multilayered media," Ph.D. dissertation, Iowa State University, 2021.
- [21] M. Schlutz, "Synthetic aperture radar imaging simulated in matlab," 2009.
- [22] J. Wang, X. Liu, and Z. Zhou, "Minimum-entropy phase adjustment for isar," *IEE Proceedings-Radar, Sonar and Navigation*, vol. 151, no. 4, pp. 203–209, 2004.
- [23] "Radarbook," <https://noffz.com/en/products/rf-test-and-simulator/radarbook/>, accessed: 2022-10-19.
- [24] "rosterial\_arduino," [http://wiki.ros.org/rosterial\\_arduino](http://wiki.ros.org/rosterial_arduino), accessed: 2022-10-19.
- [25] A. Sengupta, F. Jin, R. A. Cuevas, and S. Cao, "A review of recent advancements including machine learning on synthetic aperture radar using millimeter-wave radar," in *2020 IEEE Radar Conference (RadarConf20)*. IEEE, 2020, pp. 1–6.